Frontiers in Bioscience Landmark

Front. Biosci. (Landmark Ed) **2026**; 31(7): 52994
https://doi.org/10.31083/FBL52994

Original Research

Implantable Microsphere-Mediated Targeted Delivery of Mesenchymal Stem Cell-Derived Extracellular Vesicles Attenuates Neuroinflammation and Promotes Recovery After Cerebral Ischemia

Yiran Wang[1,†], Xiaorui Lei[1,†], Xiao Liang[1], Yiwen Huang[1], Xin Zhang[2,*], Tian Tian[1,3,*]

[1]Department of Neurobiology, School of Basic Medical Sciences, Nanjing Medical University, 211166 Nanjing, Jiangsu, China
[2]Department of Anesthesiology, The Affiliated Wuxi People's Hospital of Nanjing Medical University, 214023 Wuxi, Jiangsu, China
[3]Wuxi Medical Center, The Affiliated Wuxi People's Hospital of Nanjing Medical University, 214023 Wuxi, Jiangsu, China
*Correspondence: xinzhang3@njmu.edu.cn (Xin Zhang); ttian@njmu.edu.cn (Tian Tian)
[†]These authors contributed equally.

Academic Editors: Enrico Ragni and Thomas Heinbockel
Submitted: 16 April 2026 Revised: 28 May 2026 Accepted: 11 June 2026 Published: 24 July 2026

Abstract

Background: Ischemic stroke is a major cause of death and disability, in which neuroinflammation exacerbates injury. Mesenchymal stem cell (MSC)-derived extracellular vesicles (EVs) offer therapeutic potential but face translational hurdles in scalable production, rapid systemic clearance, and inefficient targeted delivery. **Methods:** We engineered an implantable alginate-microsphere system encapsulating EV-secreting MSCs and displaying the RGD-4C peptide (ACDCRGDCFC) on its surface. This platform functions as a bioreactor that sustains the release of functionalized EVs with enhanced targeting to the ischemic brain. Proteomics analyses compared EVs derived from 3D-microsphere cultures and conventional 2D cultures. Efficacy was evaluated in a mouse stroke model with intraperitoneal microsphere implantation, assessing biodistribution, neuroinflammation, microglial polarization, and recovery. **Results:** The system sustained the release of targeted EVs, demonstrating proteomic enrichment of anti-inflammatory cargo. *In vivo*, the platform enhanced EV accumulation in the ischemic brain, reduced neuroinflammation, shifted microglia toward a reparative phenotype, and significantly improved neuronal survival and functional recovery. **Conclusion:** This integrated platform represents a promising preclinical strategy for treating ischemic stroke and has potential applications in other neuroinflammatory diseases. This system circumvents the need for EV extraction and storage while eliminating the peak-and-trough kinetics of bolus injections, and suggests potential for future translation pending further validation.

Keywords: ischemic stroke; mesenchymal stem cells; extracellular vesicles; alginate microspheres; neuroinflammation

1. Introduction

Ischemic stroke, a major global cause of mortality and disability, triggers detrimental neuroinflammation that worsens brain injury and impairs recovery [1]. While early vascular recanalization is the standard treatment, its narrow therapeutic window fails to address the sustained inflammatory microenvironment in the ischemic penumbra [2]. Therefore, developing therapies that modulate post-stroke inflammation is an urgent clinical need. Mesenchymal stem cell (MSC)-derived extracellular vesicles (EVs) have shown promising immunomodulatory and neuroprotective effects in preclinical stroke models, largely mediated by their cargo [3,4,5]. However, clinical translation is hindered by challenges in scalable EV production, product heterogeneity, inefficient targeted delivery, and rapid systemic clearance [6]. Additional practical challenges concern the stability of EVs during storage and freeze-thaw cycles, processes which can compromise vesicle integrity, diminish bioactivity, and induce aggregation [7].

To overcome these limitations, biomaterial-based encapsulation platforms offer a powerful and innovative strategy [8]. Among them, implantable porous hydrogel microspheres, fabricated from biocompatible polymers such as alginate, present a particularly promising solution [9]. These microspheres create a protective, semi-permeable 3D niche that supports high MSC viability and sustained metabolic activity, while allowing bidirectional diffusion of nutrients and waste [10]. The feasibility and practical utility of such retrievable, sustained-release microsphere systems have already been validated in other therapeutic contexts, such as in diabetes treatment, where implanted devices are successfully removed after several days to one month without significant complications [11,12]. This establishes a translational precedent for the safe and temporary use of implantable microspheres in clinical settings [13]. Crucially, this 3D encapsulation strategy offers distinct advantages for EV-based therapy: First, it provides a physiologically more relevant 3D culture milieu that can enhance MSC paracrine function and potentially improve the yield and bioactivity of secreted EVs compared to 2D cultures [14]. Second, it

enables the sustained, and minimally invasive delivery of therapeutic EVs to the target tissue, overcoming the limitations of bolus injections. The microspheres act as a biofactory, continuously releasing EVs, which can lead to longer-lasting therapeutic effects [15].

Furthermore, a key challenge in neurotherapeutics is achieving specific homing of therapeutics to the pathologically altered tissues in the ischemic region [16]. Our previous works integrated genetic engineering to display the RGD peptide on EV surfaces [17]. RGD binds with high affinity to integrins αvβ3, which are upregulated on activated endothelium in ischemic tissue [18,19]. By combining RGD-engineered EVs with 3D microencapsulation, we developed an integrated system: the implantable microsphere acts as a local bioreactor for continuous EV production, while RGD modification directs EVs to the ischemic site, enhancing localized uptake and therapeutic efficacy.

In this study, we developed an implantable porous alginate microsphere system that functions as a 3D bioreactor, enabling the sustained release of MSC-EVs. Proteomic comparison of EVs from conventional 2D culture (2D-EVs) and microsphere-encapsulated MSCs (sph-EVs) revealed that 3D microencapsulation enriches EVs with anti-inflammatory and antioxidant stress proteins. MSCs were further engineered to stably express the RGD-4C peptide (ACDCRGDCFC) fused to a transmembrane domain, resulting in the secretion of RGD-modified EVs. Intraperitoneal implantation of these RGD-MSC-laden microspheres (RGD-MSC@Alg) in a mouse model of middle cerebral artery occlusion/reperfusion (MCAO/R) confirmed enhanced EV accumulation in the ischemic brain. Therapeutic assessment demonstrated that the platform may alleviate neuroinflammatory responses, promote neuroprotection, and facilitate early neurological recovery. This integrated biomaterial-enabled strategy combines 3D cell culture, sustained local delivery, and EV surface engineering, offering a promising preclinical approach for the treatment of ischemic stroke and related neuroinflammatory diseases.

2. Materials and Methods

2.1 Cell Culture

Human umbilical cord MSCs (passages 4-8; Vcanbio, Tianjin, China) and BV2 mouse microglia (the Type Culture Collection of Chinese Academy of Sciences) were cultured in DMEM-based media supplemented with 10% FBS (Life Technologies Corporation, Carlsbad, CA, USA) at 37 ℃ with 5% CO_2. All primary MSCs were validated for their identity by surface marker analysis using flow cytometry (**Supplementary Fig. 1**), and all primary cells and cell lines were confirmed to be free of mycoplasma contamination prior to use in experiments. To generate RGD-displaying fluorescent EVs, MSCs were transduced with a lentivirus encoding RGD-4C fused to a platelet-derived growth factor receptor transmembrane domain and tdTomato (RGD-TM-tdTomato).

2.2 Flow Cytometric Analysis

Flow cytometric analysis was performed using fluorochrome-conjugated antibodies against CD73, CD105, CD45, and HLA-DR (BioLegend, San Diego, CA, USA). Data were acquired using a BeamCyte-1026M flow cytometer (BeamCyte, Changzhou, China) and processed using the accompanying analysis software. The gating strategy was established based on the corresponding isotype controls. The MSC phenotype was characterized by the expression of positive surface markers (CD73 and CD105) and the absence of hematopoietic/immune-related markers (CD45 and HLA-DR).

2.3 Plasmid Construct and Virus Package

To enable stable RGD-4C display, the coding sequence for RGD-$(GGGGS)_2$-TM-$(GGGGS)_2$-tdTomato (or its scrambled ACDCRDGCFC as a control) with a signal sequence was synthesized (GenScript, Nanjing, China) and cloned into the lentiviral transfer vector pCSCW-IG. Lentiviral particles were produced by co-transfecting HEK293T cells with the transfer plasmid, packaging plasmid pCMVΔ8.91, and envelope plasmid pVSV-G. The supernatant was harvested 48 h post-transfection, concentrated by ultracentrifugation, and stored at –80 °C.

2.4 Encapsulation of MSCs and Viability Testing

MSCs were transduced with lentiviral vectors encoding RGD-TM-tdTomato or scrambled RDG-TM-tdTomato to display the fusion protein on the cell and EV surface. For encapsulation, cells were suspended in 1.75% (w/v) sodium alginate containing 20 μg/mL FK506 (MedChemExpress, Monmouth Junction, NJ, USA) at 2×10^7 cells/mL. Using an electrostatic droplet generator, the suspension was extruded (0.1 mL/min, 6 kV) into a 0.15 mol/L $CaCl_2$ bath to form cross-linked microspheres. After washing with phosphate-buffered saline (PBS), MSC-loaded microspheres (MSC@Alg) were cultured in complete medium. Cell viability was assessed on days 1 and 7 by Calcein-AM/PI staining (Beyotime Biotechnology, Shanghai, China) and visualized under fluorescence microscopy (Ti-E; Nikon Corporation, Tokyo, Japan).

2.5 Field-Emission Scanning Electron Microscopy (FE-SEM) Characterization of Alginate Microspheres

The cross-sectional morphology of alginate microspheres was observed using a field-emission scanning electron microscope (FE-SEM; SU8010, Hitachi, Tokyo, Japan). Samples were fixed with 2.5% glutaraldehyde, dehydrated through graded ethanol, and dried by critical point drying. The dried microspheres were frozen in liquid nitrogen and fractured to expose the internal structure. The fractured samples were mounted on conductive carbon tape, sputter-coated with gold, and imaged in secondary electron mode at an accelerating voltage of 15.0 kV and a working distance of approximately 12.8 mm. Low- and

high-magnification images were used to evaluate the overall morphology and internal porous structure of the microspheres.

2.6 In Vitro Swelling Ratio Assay of Alginate Microspheres

The swelling behavior of alginate microspheres was evaluated by monitoring the weight changes over time. Lyophilized microspheres were immersed in 1 mL PBS at 37 °C. At predetermined time points, microspheres were collected and gently blotted with filter paper to remove excess surface moisture before weighing. The swelling ratio was calculated according to the following equation:

$$Swelling\ ratio = \frac{W_t - W_d}{W_d}$$

where W_d and W_t represent the initial dry weight and swollen weight of microspheres, respectively.

2.7 In Vitro Degradation of Alginate Microspheres

Alginate microspheres with or without RGD-expressed MSCs (RGD-MSC@Alg and blank@Alg) were washed three times with deionized water and freeze-dried to determine the initial dry weight (W_0). The dried microspheres were then immersed in 1 mL PBS and incubated at 37 °C under gentle shaking. The PBS solution was refreshed every 2 days during incubation. At predetermined time points (1, 3, 5, and 7 days), microsphere samples were collected, gently washed with deionized water to remove residual salts, lyophilized, and weighed to obtain the dry weight at each time point (W_t). The remaining weight percentage was calculated according to the following equation:

$$Remaining\ weight\ (\%) = \frac{W_t}{W_0} \times 100$$

2.8 EV Isolation and Characterization

For EV collection, the standard culture medium was replaced with a medium supplemented with EV-depleted FBS. The FBS was depleted of bovine EVs *via* prior ultracentrifugation at 100,000 ×g for 18 h at 4 °C. MSCs were cultured in dishes or alginate microspheres for 48 h, and then culture supernatant was collected for EV isolation. Briefly, the supernatants underwent sequential centrifugation at 400 ×g (10 min), 2000 ×g (20 min), and 10,000 ×g (1 h) to remove cells and debris. EVs were pelleted by ultracentrifugation at 140,000 ×g for 90 min (L-80XP, Beckman Coulter, Inc., Brea, CA, USA), washed once in PBS by ultracentrifugation, and resuspended in PBS for further analysis. EV protein content was quantified by Micro BCA assay (Thermo Fisher Scientific Inc., Waltham, MA, USA). Identity and purity were confirmed *via* Western blot using antibodies against Alix and TSG101 (positive markers) and Calnexin (negative marker; all from Abcam, Cambridge, UK). Morphology was assessed by transmission electron microscopy (TEM; Tecnai G2, FEI, Hillsboro, OR, USA) after negative staining with 2% uranyl oxalate. Particle size distribution and concentration were analyzed by nanoparticle tracking analysis (NTA) using a ZetaView system (Particle Metrix, Inning am Ammersee, Germany).

2.9 EV Proteomic Profiling

Proteins extracted from 2D-EVs and sph-EVs were processed for proteomic analysis. Protein samples were digested with trypsin and analyzed via nano-LC-MS/MS using an Orbitrap Exploris 480 (Thermo Fisher) in Data-Independent Acquisition (DIA) mode. Data were processed using DIA-NN (v1.8) against the UniProt database (1% FDR). Three independent biological replicates were performed for each group, with each replicate derived from independently cultured MSCs and independently processed EVs. Raw DIA data were normalized using median normalization across all samples. No batch correction was applied, as all samples were processed in a single experimental batch. Statistical analysis was performed in R (version 4.5.2). Protein identification was controlled at a 1% false discovery rate (FDR) at both peptide and protein levels using DIA-NN built-in target-decoy strategy. For differential expression analysis, *p*-values were adjusted using the Benjamini–Hochberg method to control for multiple testing. Proteins with adjusted $p < 0.05$ and fold change >1.6 were considered significantly differentially expressed. High-expression stable proteins were prioritized based on high expression ($\log_2$ mean >75th percentile) and low variability (CV <0.3). An importance score, (μ/μ_max) × [1/(CV + 0.1)], was used for ranking. Differentially expressed proteins (DEPs) were identified with an adjusted $p < 0.05$ and fold change >1.6. Functional enrichment analysis of Gene Ontology (GO) terms and Kyoto Encyclopedia of Genes and Genomes (KEGG) pathways was performed using the ClusterProfiler R package (version 4.5.2, Bioconductor, Buffalo, NY, USA).

2.10 EV Uptake Assay

EVs were harvested from three distinct sources: (1) conventionally 2D-cultured MSCs expressing RDG-TM-tdTomato (RDG-2D-EVs); (2) microsphere-encapsulated MSCs expressing RGD-TM-tdTomato (RGD-sph-EVs); and (3) microsphere-encapsulated MSCs expressing the control RDG-TM-tdTomato (RDG-sph-EVs). BV2 cells were labeled with CellTracker Green CMFDA (Life Technologies) and incubated with EVs (2×10^9/mL) for 3 h. Cells were fixed, stained with DAPI (Sigma-Aldrich, St. Louis, MO, USA), and imaged using a confocal microscope (LSM880, Zeiss, Jena, Germany). Image analysis was performed with Fiji software (ImageJ, version 1.54p, National Institutes of Health, Bethesda, MD, USA) under consistent settings. Fluorescence intensities per cell were quantified from six random fields per experiment.

2.11 Experimental Animals

Adult male C57BL/6 mice were provided by the Animal Core Facility of Nanjing Medical University (Nanjing, China). Mice were randomly assigned to experimental groups using a computer-generated randomization method. All animal experiments were approved by the Animal Care and Use Committee of Nanjing Medical University (IACUC2411052) and carried out in accordance with institutional guidelines. Mice were anesthetized with isoflurane (induction at 3–4% and maintenance at 1.5–2% in oxygen) during all surgical procedures. Focal cerebral ischemia was induced by MCAO. A 6-0 nylon suture was advanced into the right internal carotid artery to occlude the MCA origin for 30 min, followed by reperfusion. Successful occlusion was confirmed by a 75–90% reduction in cerebral blood flow measured using laser Doppler flowmetry. Sham-operated mice underwent the same procedure without arterial occlusion. Six hours after reperfusion, mice were re-anesthetized with isoflurane, and a midline abdominal incision was performed to access the peritoneal cavity. Approximately 1.2×10^4 MSC-loaded microspheres were implanted intraperitoneally, and the incision was closed with absorbable sutures. For EV tracking, mice were euthanized 72 h post-implantation by intraperitoneal injection of sodium pentobarbital at an overdose dose (150 mg/kg body weight; prepared at 50 mg/mL), followed by cervical dislocation to ensure death. Brains were then harvested, fixed, and imaged *ex vivo* using an IVIS Spectrum system (PerkinElmer, Shelton, Connecticut, USA).

2.12 TTC Staining and Infarct Volume Analysis

Brain infarct volume was assessed using 2,3,5-triphenyltetrazolium chloride (TTC) staining (n = 6 mice per group). Brains were collected and cut into 2-mm-thick coronal sections. The sections were incubated in 2% TTC solution at 37 °C for 15 min in the dark and then fixed in 4% paraformaldehyde (PFA). Viable tissue was stained red, whereas infarcted tissue remained white. Infarct areas were quantified using Fiji software (version 1.54p, National Institutes of Health, Bethesda, MD, USA). Infarct volume quantification was performed by investigators blinded to treatment group allocation. To correct for cerebral edema, corrected infarct area was calculated as follows:

$$\text{Corrected infarct area} = \text{contralateral hemisphere area} - \text{ipsilateral non-infarct area}$$

Total infarct volume was calculated by summing the corrected infarct areas of all slices and multiplying by slice thickness (2 mm), and was expressed as a percentage of the contralateral hemisphere volume.

2.13 Immunofluorescence Staining and Confocal Imaging

After 6 h of reperfusion following MCAO/R, mice received intraperitoneal implantation of MSC@Alg or RGD-MSC@Alg. Blank alginate microspheres (blank@Alg) were implanted as a control. Seventy-two hours later, mice were perfused with PBS followed by 4% paraformaldehyde. Brains were collected and sectioned at 40 μm (n = 6 mice per group). Sections were permeabilized with 0.3% Triton X-100, blocked with 3% BSA, and incubated overnight at 4 °C with anti-GFAP, anti-MAP2 and anti-Iba-1 antibodies (Abcam). After incubation with Alexa Fluor 488 conjugated secondary antibodies, sections were stained with DAPI and mounted with antifade reagent. Images were acquired using an LSM880 confocal microscope and analyzed with Fiji software. Imaging and analysis parameters were kept constant across groups. The fluorescence intensities of tdTomato in the ischemic region and Iba-1 per cell were collected from six random imaging fields for each independent experiment and averaged.

2.14 Quantitative Real-Time PCR (RT-qPCR) and Enzyme-Linked Immunosorbent Assay (ELISA)

Seventy-two hours post-implantation, ischemic brain tissue was collected according to the demarcated area from previous reports (n = 6 mice per group) [17,20]. Total RNA was extracted using TRIzol reagent (Invitrogen, Carlsbad, CA, USA). After quality assessment, cDNA was synthesized with a PrimeScript RT kit (Takara, Kusatsu, Shiga, Japan). qPCR was performed on a LightCycler 96 system (Roche, Switzerland) using SYBR Green Master Mix (Vazyme, Nanjing, Jiangsu, China). mRNA levels of polarization markers (CD206, CD86, iNOS, Arg1) were analyzed *via* the $2^{-\Delta\Delta Ct}$ method normalized to β-actin and sham controls. For cytokine quantification, tissue homogenates were centrifuged at 12,000 ×g for 20 min (n = 6 mice per group). Levels of tumor necrosis factor-α (TNF-α), interleukin-1β (IL-1β), and interleukin-6 (IL-6) were measured by ELISA (MultiSciences Biotech Co., Ltd., Hangzhou, Zhejiang, China) following the manufacturer's protocol.

2.15 Nissl Staining and Neurobehavioral Tests

Neuronal survival was evaluated at day 7 after reperfusion by Nissl staining using 0.5% cresyl violet (Sigma-Aldrich), followed by dehydration and mounting (n = 3 mice per group). Neurological function was assessed daily for 7 days using the modified Neurological Severity Score (mNSS, 0–18 scale), which integrates motor, sensory, reflex, and balance tests (n = 6 mice per group). Higher scores reflect greater impairment. Motor coordination was evaluated by the rotarod test (n = 6 mice per group). Mice were pretrained for three days on the rotarod (16 revolutions per minute), and the latency to fall was recorded over three trials per animal.

2.16 Statistical Analysis

Data are presented as mean ± standard error of the mean (SEM). For all experiments, n value refers to the num-

ber of independent biological replicates, defined as separate experimental runs using independently prepared cell cultures or distinct animal subjects. Details of biological replicate numbers for each experiment are specified in the corresponding Figure legends. Technical replicates were used to assess assay precision and averaged before statistical analysis. For EV quantification, RT-qPCR, and rotarod tests, three technical replicates were analyzed per experiment. ELISA measurements were performed in six technical replicates and averaged. Immunofluorescence quantification was based on six randomly selected fields per sample. Statistical analysis was conducted with GraphPad Prism 9.0 (GraphPad Software Inc., San Diego, CA, USA). Group comparisons were made using unpaired *t*-test (two groups) or one-/two-way Analysis of Variance (ANOVA) with Tukey's post-hoc test (multiple groups). Statistical significance was defined as $p < 0.05$. Prior to parametric statistical analyses, data distribution normality was assessed using the Shapiro–Wilk test.

3. Results

3.1 Fabrication and Sustained Release Profile of Implantable MSC-Laden Alginate Microspheres

To develop a sustained delivery platform for MSC-derived EVs, we fabricated cell-laden alginate microspheres using an electrostatic spraying technique (Fig. 1A). The sodium alginate solution was co-formulated with the immunomodulatory drug FK506, which is known to locally suppress T-cell activation and macrophage-driven fibrogenesis [21]. This method enabled the generation of uniform, implantable microspheres with an average diameter of approximately 250 μm and high cell encapsulation efficiency (Fig. 1B). Live/Dead staining (Calcein-AM/PI) demonstrated that the encapsulated MSCs remained highly viable throughout a 7-day culture period (Fig. 1C). This confirms the cytocompatibility of the alginate-FK506 matrix and the electrostatic spraying process, ensuring a source of viable cells for continuous EV production. The structural and physicochemical properties of the microspheres were further characterized. SEM images confirmed that both intact and cross-sectioned MSC@Alg microspheres maintained a uniform and well-defined spherical morphology (Fig. 1D). High-magnification cross-sectional images revealed an interconnected porous network, which may facilitate nutrient diffusion, cell survival, and EV release. In PBS at 37 °C, blank@Alg and MSC@Alg microspheres exhibited similar swelling profiles before reaching equilibrium (Fig. 1E), indicating that MSC encapsulation did not alter matrix hydration properties. Both groups also showed gradual and comparable degradation behavior, with approximately 15–20% mass loss over 7 days (Fig. 1F), demonstrating favorable structural stability and controlled degradability. To evaluate sustained EV secretion, MSC-laden microspheres were incubated in culture medium and EV release was monitored over time. EV release in the supernatant increased in a near-linear manner during the first 6 days (measured at 2-day intervals) before declining at day 8 (Fig. 1G). Collectively, these findings indicate that the MSC@Alg microsphere system can maintain MSC viability while enabling prolonged EV release.

3.2 Comparative Analysis of EVs From Microencapsulated and Planar-Cultured MSCs

To assess the impact of microencapsulation on EV biogenesis, we compared the yield of 2D-EVs versus sph-EVs. After 48 h of culture under each condition, EVs were isolated using identical protocols and analyzed by NTA. Microencapsulation significantly increased EV production, yielding approximately 2.1-fold more particles than 2D culture (Fig. 2A). To investigate the impact of the microencapsulation microenvironment on EV molecular profiles, we conducted comparative proteomics of 2D-EVs and sph-EVs. High-expression stable proteins were selected for analysis. Both proteomes exhibited substantial overlap with the ExoCarta top 100 exosomal markers [22], confirming EV identity (Fig. 2B). GO and KEGG analyses indicated a common core signature enriched in extracellular matrix organization, wound healing, hemostasis, and cell-substrate adhesion (**Supplementary Fig. 2A–H**). The sph-EV proteome was specifically enriched in cell-matrix adhesion, integrin-mediated signaling, inflammation modulation, and dynamic cellular responses. These findings suggest that sph-EVs may be associated with pathways related to adhesion, cell survival, motility, and inflammation modulation.

Direct quantitative comparison between sph-EV and 2D-EV proteomes indicated distinct differentially expressed proteins (DEPs), predominantly upregulated in sph-EVs (Fig. 2C). Key upregulated proteins included integrin subunits, MFGE8, and HSPD1, all involved in cell–matrix interactions and signaling. GO analysis highlighted enrichment in processes related to dynamic adhesion and morphology, such as cell–substrate adhesion, substrate adhesion-dependent spreading, and integrin-mediated signaling (Fig. 2D). Enrichment was also observed in cytoplasmic translation and intracellular transport, indicating enhanced biosynthetic and trafficking activity in encapsulated MSCs (**Supplementary Fig. 3A,B**). KEGG pathway analysis further identified Focal adhesion, Integrin signaling, PI3K-Akt signaling, and Regulation of actin cytoskeleton as the most enriched pathways (Fig. 2E), suggesting that sph-EVs may be associated with recipient cell adhesion, survival, and cytoskeletal dynamics.

Unsupervised clustering showed sph-EVs were enriched in key functional protein groups. Anti-inflammatory mediators, including Annexins (ANXA1-4) [23] and tissue inhibitors of metalloproteinases (TIMP1-3) [24], were prominently upregulated (Fig. 2F). Proteins involved in EV biogenesis and trafficking, such as ESCRT components (ALIX, VPS28), tetraspanins (CD9, CD63, CD81), and membrane trafficking factors (RAB35, SNAP23, VAMP3)

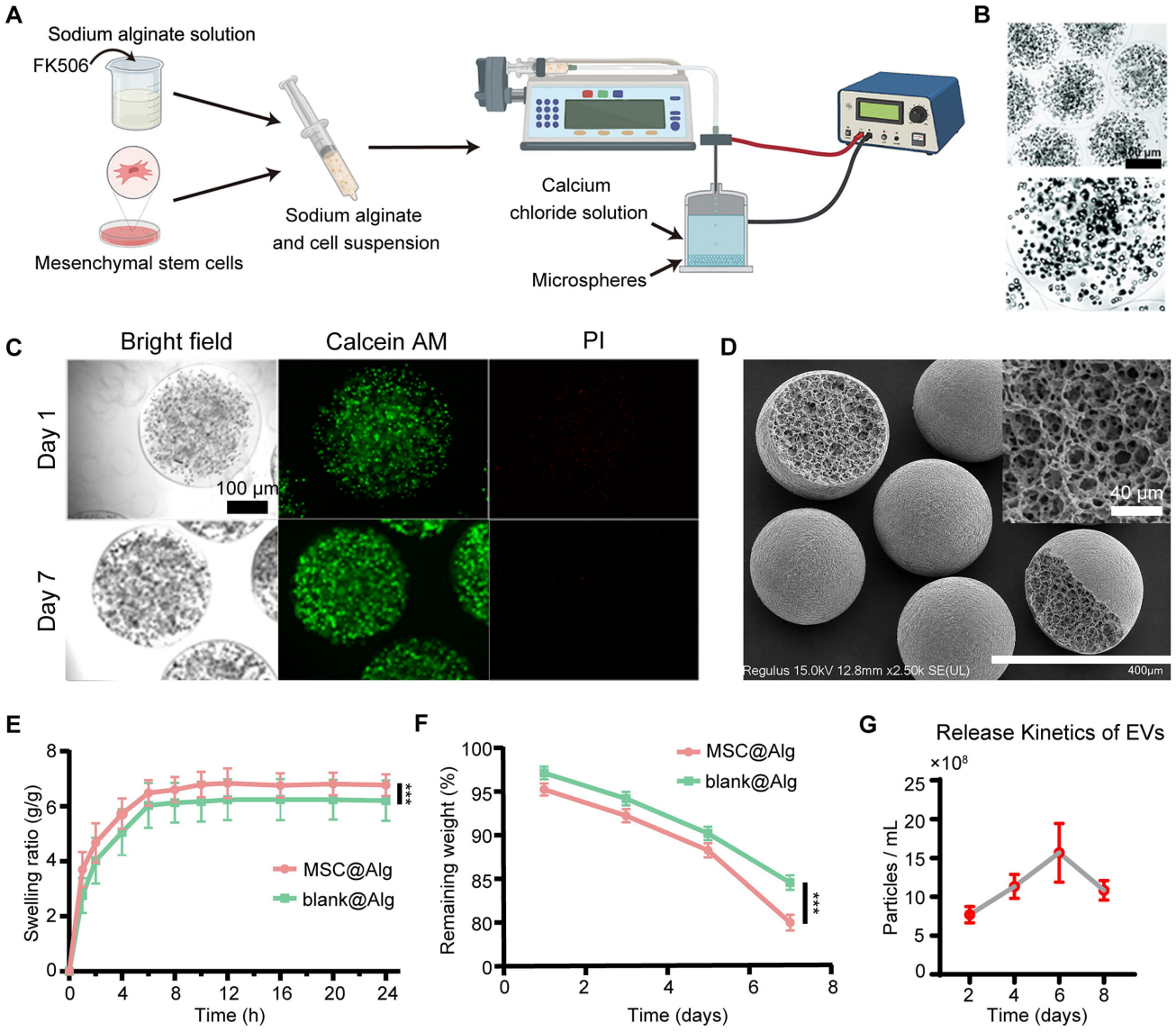

Fig. 1. Fabrication and EV release profiling of MSC-laden alginate microspheres. (A) Schematic of the preparation of MSC-laden alginate microspheres *via* electrostatic spraying. (B) Representative bright field images of alginate microsphere encapsulating MSCs. Scale bar, 100 μm. (C) Viability assessment of encapsulated MSCs over a 7-day culture period. Representative fluorescence images show live cells stained with Calcein-AM (green) and dead cells stained with propidium iodide (red). Scale bar, 100 μm. (D) Representative SEM images of intact and deliberately cross-sectioned MSC@Alg microspheres. Scale bar, 400 μm. Upper right inset: higher-magnification view of the cross-section showing internal porous structure. Scale bar, 40 μm. (E) Swelling ratios of blank@Alg and MSC@Alg microspheres over 24 h in PBS at 37 °C. Data are presented as mean ± SEM (n = 3 independent experiments, with at least 10 microspheres measured per time point). Statistical analysis was performed using two-way ANOVA followed by Tukey's post hoc test. $^{***}p < 0.001$. (F) *In vitro* degradation profiles were measured by mass loss over 7 days. Both formulations showed approximately 15–20% mass loss by day 7. Data are presented as mean ± SEM (n = 3 independent experiments). Statistical significance was determined by two-way ANOVA followed by Tukey's post hoc test, $^{***}p < 0.001$. (G) Release kinetics of EVs from alginate microsphere-encapsulated MSCs. EV concentration in the culture medium was measured every 48 h over an 8-day period. Data are presented as mean ± SEM (n = 6 independent experiments). MSC, Mesenchymal stem cell; EV, extracellular vesicle; SEM, Scanning Electron Microscopy; ANOVA, Analysis of Variance.

[25], were also comprehensively elevated (Fig. 2G). Additionally, 23 antioxidant/stress response proteins were upregulated, with 7 reaching significance, including chaperones (HSPD1, HSPA1B, HSPA8, HSP90AA1) [26] and redox enzymes (SOD2, GCLC, PRDX5) [27] (Fig. 2H). While upward trends were observed for growth factors

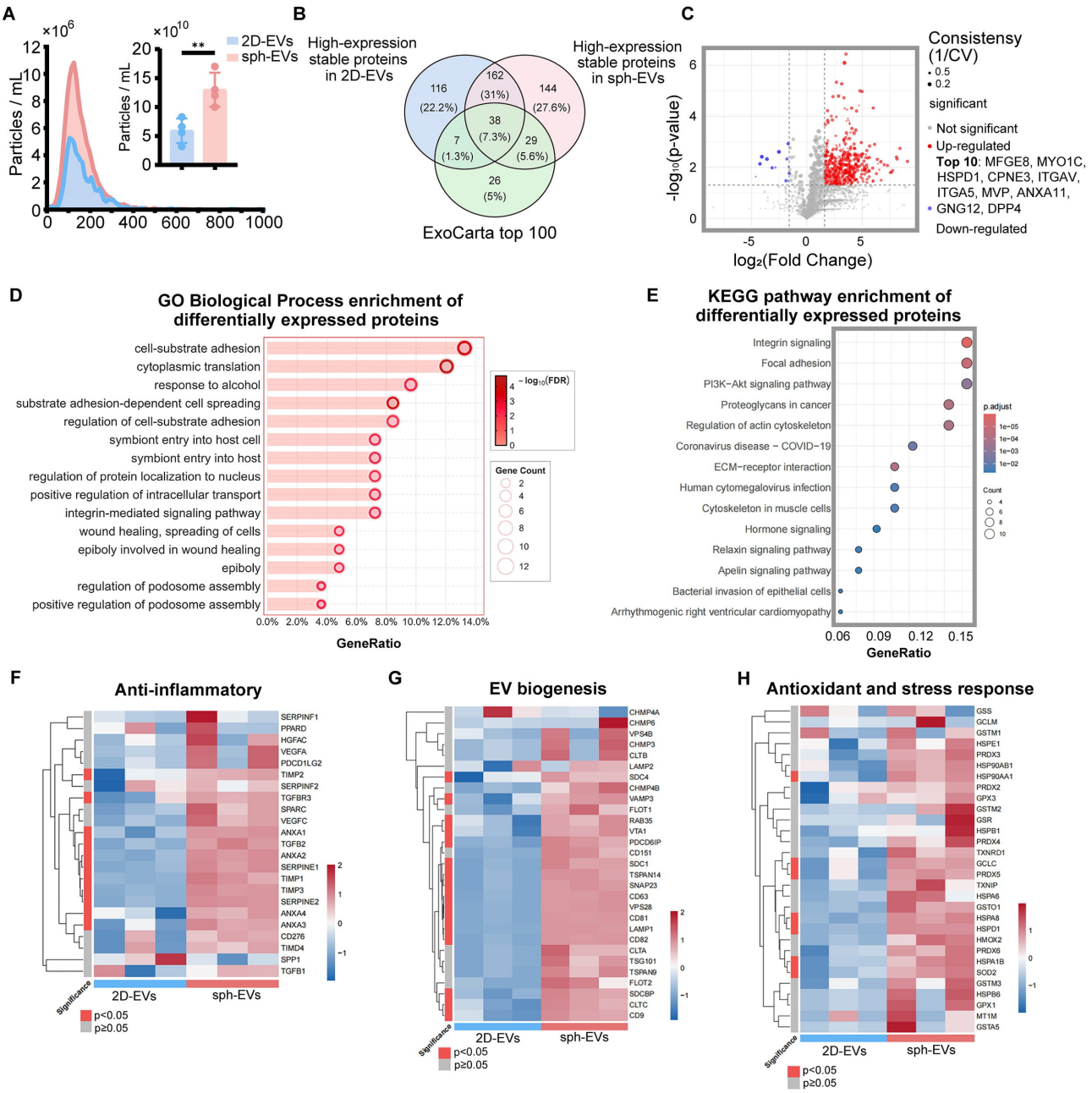

Fig. 2. Yield comparison and proteomic profiling of proteins of 2D-EVs and sph-EVs. (A) Quantitative comparison of the yield (n = 4 independent EV preparations) of 2D-EVs and sph-EVs. Data are presented as mean ± SEM. Statistical significance was determined by Student's *t*-test ($^{**}p < 0.01$). Representative NTA profiles are shown. (B) Venn analysis of high-expression stable proteins in 2D-EVs and sph-EVs compared with the top 100 proteins from the ExoCarta database. (C) Volcano plot of significantly up- and down-regulated proteins in sph-EVs compared with 2D-EVs. The dot size is proportional to the consistency of detection, represented by the inverse of the coefficient of variation (1/CV). (D,E) Top 15 enriched GO Biological Processes (D) and KEGG pathways (E) for differentially expressed proteins in 2D-EVs versus sph-EVs. (F–H) Unsupervised clustering of proteins differentially abundant between 2D-EVs and sph-EVs within key functional categories: (F) anti-inflammatory, (G) EV biogenesis, and (H) antioxidant/stress response. Abundance is represented as row Z-score of standardized spectral counts. An annotation bar color-codes each protein based on its statistical significance (red: significant, adjusted *p*-value < 0.05; gray: non-significant). NTA, nanoparticle tracking analysis; GO, Gene Ontology; KEGG, Kyoto Encyclopedia of Genes and Genomes.

and neuroregeneration-related proteins, these changes were not statistically significant (**Supplementary Fig. 4A,B**), and minimal alteration was detected in anti-apoptotic proteins. Collectively, microencapsulation enriches sph-EVs with proteins associated with anti-inflammatory and EV biogenesis-related functions.

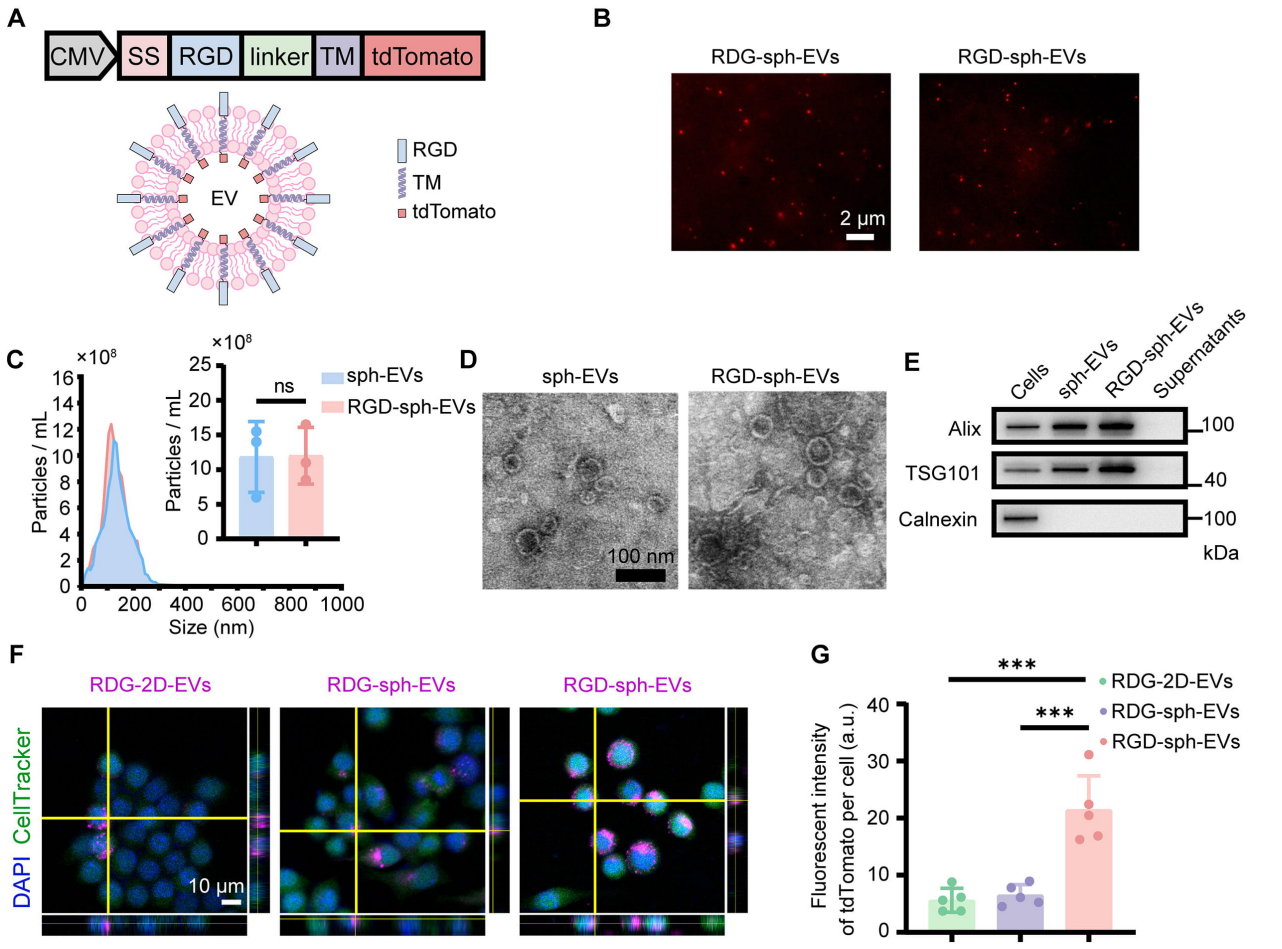

Fig. 3. Preparation and characterization of RGD-sph-EVs. (A) Schematic diagram of preparation of RGD-EVs by expressing designing RGD-TM-tdTomato sequence in MSCs. The sequence consists of a signal sequence (SS) for secretion, RGD-4C peptide sequence (RGD), linker sequence (2 × GGGGS), transmembrane domain (TM), and tdTomato tags. (B) Isolated RDG-sph-EVs or RGD-sph-EVs present small particles (Red) on fluorescent image. Scale bar, 2 μm. (C) Quantitative comparison of the yield (n = 3 independent EV preparations) of sph-EVs and RGD-sph-EVs. Data are presented as mean ± SEM. No statistical significance was determined by Student's *t*-test. Representative nanoparticle tracking analysis profiles are shown. ns, not significant. (D) Representative TEM images of sph-EVs and RGD-sph-EVs. Scale bar, 100 nm. (E) Western blot analysis of Alix, TSG101, and Calnexin from MSCs, sph-EVs, RGD-sph-EVs, and supernatant obtained from the ultracentrifugation. (F) Representative confocal images of cellular uptake of 2D-EVs expressing RDG-TM-tdTomato, or sph-EVs expressing RDG/RGD-TM-tdTomato after 3-h incubation with BV2 microglia. Red shows tdTomato signal (EVs). Green indicates cell profile. Blue is nuclei. Scale bar, 10 μm. (G) Quantification of intracellular tdTomato fluorescence intensity (n = 5 independent uptake assays) corresponding to the EV uptake shown in (F). Data are presented as mean ± SEM. Statistical significance was determined by one-way ANOVA followed by Tukey's post hoc test. $^{***}p < 0.001$.

3.3 Engineering MSC-EVs With Enhanced Targeting Capability Through Surface Expression of RGD Peptide

To enhance targeting, we engineered sph-EVs to display RGD-4C, a peptide that binds integrin αvβ3 upregulated in the ischemic brain. A fusion construct (RGD-TM-tdTomato) was designed by linking the RGD-4C sequence to a transmembrane domain and a tdTomato reporter, preceded by a signal peptide for secretion (Fig. 3A). A scrambled RDG version served as a control. MSCs were stably transduced to express these constructs prior to 2D culture or microencapsulation, generating RDG-2D-EVs, RDG-sph-EVs, and RGD-sph-EVs. tdTomato fluorescence confirmed surface display (Fig. 3B). RGD modification did not alter EV yield, size, morphology, or marker expression (Alix, TSG101; Calnexin-negative) (Fig. 3C–E). Functional uptake assays in BV2 microglial cells revealed markedly enhanced internalization of RGD-sph-EVs after 3 h, with tdTomato signal approximately 4-fold higher than RDG-sph-EV and RDG-2D-EV controls (Fig. 3F,G). These results demonstrate that RGD functionalization effectively promotes EV uptake by integrin αvβ3-expressing cells without interfering with microencapsulation-enhanced EV biogenesis.

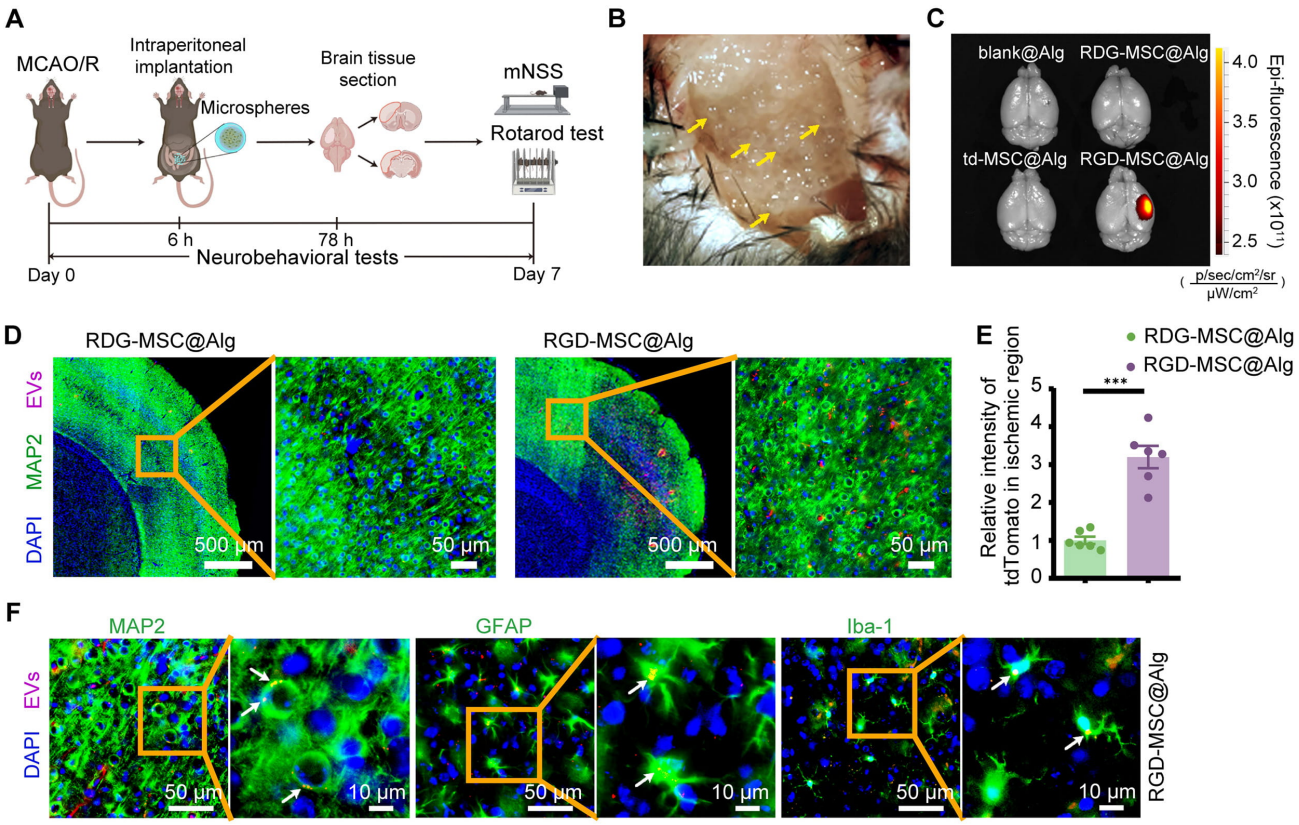

Fig. 4. ***In vivo*** **delivery of EVs from intraperitoneally implanted RGD-MSC@Alg to ischemic brain**. (A) Schematic of the experimental design. Mice underwent MCAO/R, followed by intraperitoneal implantation of MSC-laden alginate microspheres 6 h after reperfusion. The timeline illustrates the key procedures and endpoint. (B) Representative photos of alginate microspheres placed in the peritoneal cavity. Yellow arrows point to microspheres. (C) Representative *ex vivo* fluorescence images (overlaid with photographs) of mouse brains from different experimental groups at 72 h post-implantation (78 h post-reperfusion). Mice received either blank alginate microspheres or microspheres encapsulating MSCs stably expressing tdTomato (control), RDG-TM-tdTomato (non-targeting), or RGD-TM-tdTomato (targeting). (D) Representative fluorescence images showing the distribution of tdTomato-labeled EVs (red) and the neuronal marker MAP2 (green) in the ischemic cortical area. Images are from mice implanted with microspheres containing MSCs expressing either RDG-TM-tdTomato or RGD-TM-tdTomato. Scale bar, 500 μm and 50 μm. (E) Quantification of tdTomato fluorescence intensity in the ischemic region, corresponding to the EV signal in images such as (D). Data are presented as mean ± SEM (n = 6 biologically independent animals). $^{***}p < 0.001$ by one-way ANOVA with Tukey's post hoc test. (F) Representative confocal images demonstrating cellular association of RGD-sph-EVs (red) in the peri-infarct cortex. Arrows indicate that EVs are co-localized with markers for neurons (MAP2), astrocytes (GFAP), and microglia (Iba-1) (all in green). Scale bar, 50 μm and 10 μm. MCAO/R, middle cerebral artery occlusion/reperfusion; MAP2, microtubule-associated protein 2.

3.4 Intraperitoneally Implanted RGD-MSC@Alg Enable Targeted Delivery of EVs to the Ischemic Brain

We next sought to validate their targeted delivery *in vivo* using an intraperitoneal implantation route and a mouse model of MCAO/R (Fig. 4A,B). Alginate microspheres encapsulating engineered MSCs were implanted intraperitoneally 6 h after reperfusion. To evaluate the delivery of EVs to the brain, we first employed *ex vivo* imaging of brain tissues harvested 72 h post-implantation. Mice receiving blank@Alg, or MSCs expressing cytosolic tdTomato (td-MSC@Alg) or the non-targeting RDG-TM-tdTomato (RDG-MSC@Alg) showed minimal background fluorescence in the ischemic hemisphere (Fig. 4C). Strikingly, brains from mice that received RGD-MSC@Alg microspheres displayed an increased accumulation of signal specifically in the ipsilateral ischemic hemisphere. This finding suggests that the RGD modification, when produced within the microsphere platform, may confer enhanced tropism for the ischemic brain region following intraperitoneal implantation.

We further corroborated this finding at the cellular level using confocal microscopy. In the ischemic cortical area, tdTomato-labeled EVs from the RGD-MSC@Alg group were abundantly distributed (Fig. 4D). Quantification of this signal confirmed a significantly higher accumulation of RGD-displayed EVs in the ischemic region

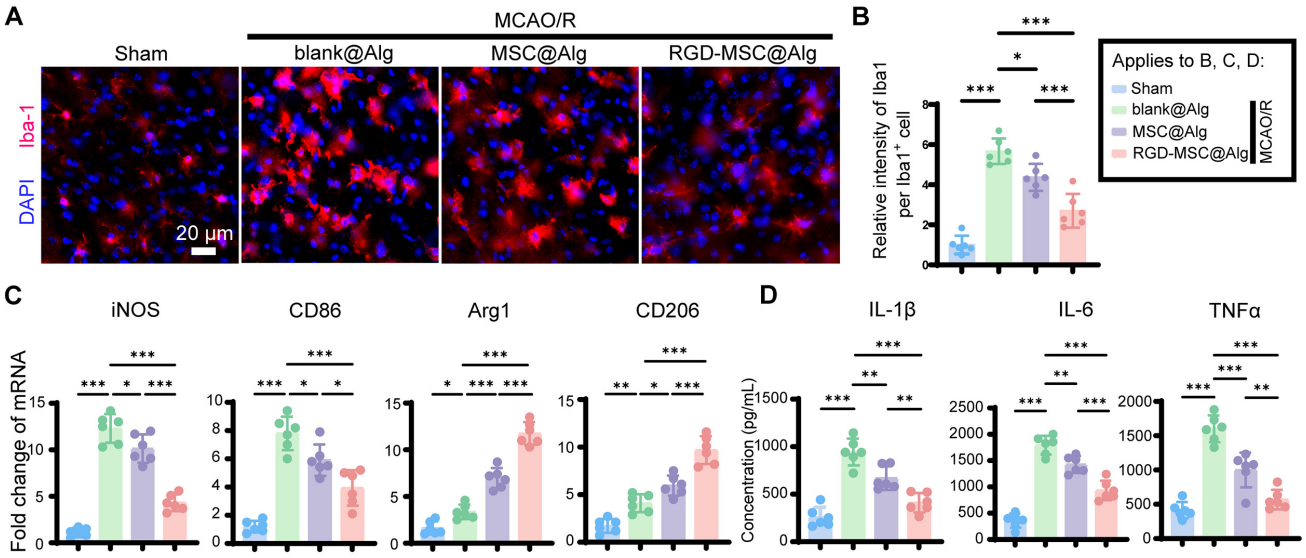

Fig. 5. RGD-MSC@Alg intraperitoneal implantation attenuates post-ischemic neuroinflammation. MSC@Alg and blank@Alg were used as controls. (A) Representative immunofluorescence images of Iba1$^+$ microglia in the cortical peri-infarct region at 72 h post-implantation (78 h post-reperfusion). Scale bar, 20 μm. (B) Quantitative analysis of fluorescence intensity of Iba1 per cell. Data are expressed as mean ± SEM (n = 6 biologically independent animals). (C) mRNA expression levels of microglial polarization markers in the ipsilateral ischemic tissue at 72 h post-implantation. Gene expression of pro-inflammatory markers (iNOS, CD86) and anti-inflammatory markers (Arg1, CD206) was quantified by RT-qPCR. Data are presented as mean ± SEM (n = 6 biologically independent animals). (D) Protein levels of pro-inflammatory cytokines (IL-1β, IL-6, TNF-α) in the supernatant of homogenized ischemic hemisphere tissue at 72 h post-implantation, as determined by ELISA. Data are presented as mean ± SEM (n = 6 biologically independent animals). Statistical analysis: For all panels, data were analyzed by one-way ANOVA with Tukey's post hoc test. $^*p < 0.05$, $^{**}p < 0.01$, $^{***}p < 0.001$. iNOS, inducible nitric oxide synthase; CD86, cluster of differentiation 86; Arg1, arginase 1; RT-qPCR, Quantitative Real-Time PCR; IL-1β, interleukin-1β; IL-6, interleukin-6; TNF-α, tumor necrosis factor-α; ELISA, Enzyme-Linked Immunosorbent Assay.

compared to the scrambled RDG control (Fig. 4E). High-resolution imaging revealed that these RGD-sph-EVs were not merely present in the parenchyma but were detected within key neural cell populations. As shown in Fig. 4F, tdTomato-positive puncta were found co-localized with neurons (MAP2$^+$), astrocytes (GFAP$^+$), and microglia (Iba-1$^+$), suggesting cellular association of EV-derived signals with major neural cell types in the brain. Collectively, these *in vivo* data indicate that the intraperitoneally implanted RGD-MSC@Alg continuously produces and systemically releases RGD-functionalized EVs. These EVs have the ability to home to the site of cerebral ischemia and are efficiently taken up by the relevant neural cells.

3.5 Intraperitoneal Implantation of RGD-MSC@Alg Significantly Attenuates Post-Ischemic Neuroinflammation

We next assessed the therapeutic efficacy of intraperitoneally implanted RGD-MSC@Alg in modulating neuroinflammation after MCAO/R. Mice received implants 6 h post-reperfusion (blank@Alg, MSC@Alg, or RGD-MSC@Alg). At 72 h, immunofluorescence in the peri-infarct cortex revealed that Iba1$^+$ microglia in the RGD-MSC@Alg group displayed less activated morphology compared to controls (Fig. 5A). Quantification confirmed a significant reduction in Iba1 intensity in the RGD-MSC@Alg group versus both control groups (Fig. 5B).

RT-qPCR of ischemic brain tissue showed that RGD-MSC@Alg implantation markedly downregulated pro-inflammatory markers (iNOS, CD86) and upregulated anti-inflammatory/reparative markers (Arg1, CD206), with a more pronounced shift toward an M2-like phenotype than in the MSC@Alg group (Fig. 5C). ELISA further demonstrated significantly lower levels of IL-1β, IL-6, and TNF-α in the RGD-MSC@Alg group compared to controls (Fig. 5D). Together, these data indicate that intraperitoneal RGD-MSC@Alg implantation effectively attenuates post-stroke neuroinflammation by reducing microglial activation and promoting a reparative phenotypic switch.

3.6 RGD-MSC@Alg Intraperitoneal Implantation Promotes Neuroprotection and Functional Recovery After Ischemic Stroke

We next evaluated the neuroprotective effects of RGD-MSC@Alg microspheres in MCAO/R mice. Following intraperitoneal implantation at 6 h post-stroke, the microspheres retained their structural integrity for at least 7 days (**Supplementary Fig. 5A**). TTC staining at day 3 after reperfusion demonstrated that RGD-MSC@Alg treatment significantly reduced cerebral infarct volume compared

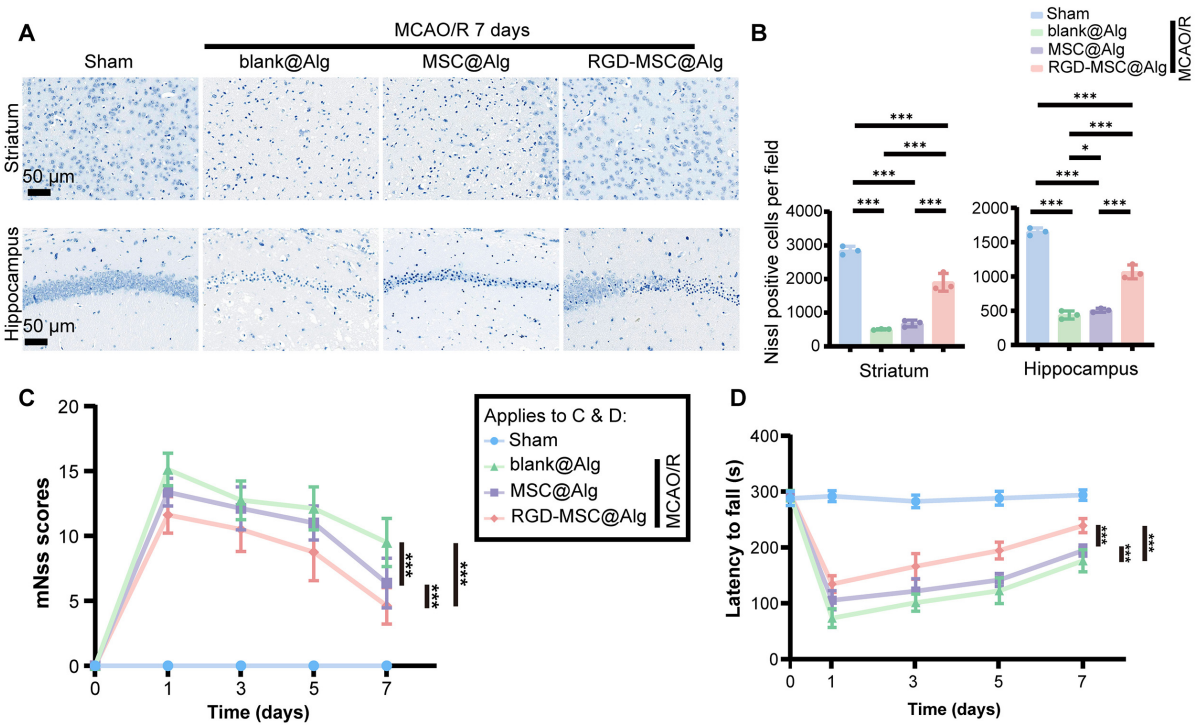

Fig. 6. Implantation of RGD-MSC@Alg confers neuroprotection and promotes functional recovery after stroke. (A) Representative Nissl-stained images of the vulnerable striatum and hippocampal CA1 regions in the ipsilateral hemisphere on day 7 post-reperfusion. Mice received intraperitoneal implantation of blank@Alg, MSC@Alg, or RGD-MSC@Alg at 6 h post-reperfusion. Scale bar, 50 μm. (B) Quantification of surviving neurons (Nissl-positive cells) per field in the striatum and hippocampal CA1 region, corresponding to the images in (A). Data are expressed as mean ± SEM (n = 6 biologically independent animals). $^{*}p < 0.05$, $^{***}p < 0.001$ by One-way ANOVA with Tukey's post hoc test. (C,D) Longitudinal assessment of neurological and motor function recovery. (C) mNSS and (D) latency to fall on a rotarod were evaluated over 7 days post-reperfusion. Data are expressed as mean ± SEM (n = 6 biologically independent animals). Data are expressed as mean ± SEM. $^{***}p < 0.001$ by Two-way ANOVA.

with blank@Alg and MSC@Alg controls (**Supplementary Fig. 5B,C**). Consistent with these findings, Nissl staining at day 7 revealed markedly reduced lesion areas and improved neuronal survival in the striatum and hippocampal CA1 regions in the RGD-MSC@Alg group (Fig. 6A,B), indicating significant neuroprotection against ischemic neuronal death. Neurological function was further assessed over a 7-day period. Mice treated with RGD-MSC@Alg exhibited accelerated and more complete functional recovery, as evidenced by significantly lower mNSS scores at days 3, 5, and 7 (Fig. 6C). In addition, motor coordination assessed by the rotarod test was showed improvement in the RGD-MSC@Alg group, with longer latencies to fall observed from day 3 onward (Fig. 6D). Collectively, these results demonstrate that the implantable RGD-MSC@Alg microsphere system provides sustained neuroprotection and effectively promotes functional recovery after ischemic stroke.

4. Discussion

The development of this implantable alginate microsphere system provides an alternative strategy to address key translational challenges of conventional MSC-EV therapy, including scalability, stability, cost, and pharmacokinetics [28]. Unlike conventional methods that require large-scale EV isolation, cold-chain storage, and repeated administration, our platform serves as an *in situ* "living factory," enabling sustained EV release and bypassing complex downstream processing. Compared with intravenous injection, intraperitoneal implantation may enable more sustained delivery and altered EV cargo profiles through 3D encapsulation, providing a preliminary preclinical strategy for EV-based therapies.

Recent comprehensive reviews have established that MSC-derived EVs promote neuroprotection, reduce neuroinflammation, preserve blood-brain barrier integrity, and enhance neurogenesis and angiogenesis in ischemic stroke [29]. However, clinical translation has been hindered by several persistent barriers, including batch-to-batch variability, suboptimal and inconsistent EV yield, rapid systemic clearance within minutes to hours after administration, lack of sustained delivery, and inefficient targeting to ischemic lesions [30]. Our platform addresses multiple limitations simultaneously. First, 3D microencapsulation yields approximately 2.1-fold more EVs than

conventional 2D culture, consistent with reports that 3D culture systems better recapitulate the *in vivo* microenvironment and enhance MSC paracrine activity through altered mechanotransduction and cell-matrix interactions [31]. Second, proteomic profiling suggests that sph-EVs are enriched with functionally relevant anti-inflammatory mediators (Annexin A1-4, TIMP1-3) and antioxidant stress proteins (SOD2, HSPD1, PRDX5, GCLC) compared to 2D-EVs. This enrichment is noteworthy because Annexin A1 has been identified as a key mediator of inflammation resolution by promoting neutrophil apoptosis and macrophage efferocytosis [32], while TIMPs exert neuroprotective effects beyond matrix metalloproteinase inhibition, including direct modulation of inflammatory signaling in microglia [33]. Third, the sustained release profile from implantable microspheres addresses the rapid clearance issue inherent to bolus administration, which typically results in minimal EV retention beyond 24–48 h [30]. It is worth noting that direct comparison of therapeutic efficacy across studies remains challenging due to heterogeneity in EV isolation methods, dosing regimens, administration routes, and stroke models [34]. The present study has several points that merit discussion. We did not include a comparator group treated with conventionally administered isolated EVs, such as intravenous or intranasal delivery. While the implantable system demonstrates sustained local release and enhanced targeting to the ischemic brain, whether this approach confers superior therapeutic efficacy compared to optimized regimens of bolus EV administration remains to be established. Future head-to-head comparative studies with standard routes of EV delivery will be necessary to rigorously evaluate the relative advantages and limitations of this implantable platform. Although our proteomic analysis identified enrichment of anti-inflammatory-associated proteins in sph-EVs, causality between specific enriched proteins and the observed *in vivo* effects remains to be established through targeted loss- or gain-of-function studies.

Biomaterial-assisted EV delivery has emerged as a strategy to enhance therapeutic outcomes by enabling controlled release, protecting EVs from degradation, and improving local retention [35]. Hydrogels, microspheres, scaffolds, and depots have been explored for EV delivery in various disease contexts, including myocardial infarction, wound healing, cartilage repair, and CNS disorders [36]. For CNS applications, injectable hydrogels have been used to achieve sustained EV release following intracerebral or intrathecal administration, though these routes carry inherent risks of needle-related tissue damage [37,38]. Our alginate microsphere platform offers distinct advantages over existing biomaterial approaches. Unlike injectable hydrogels that disperse at the injection site and are not readily retrievable, our discrete microspheres are retrievable, a potentially advantageous feature for safety monitoring and potential therapy termination. The porous alginate matrix supports high MSC viability and metabolic activity over at least 7 days, serving as a sustained *in situ* production system for continuous EV release. This distinguishes our approach from systems that pre-load isolated EVs into biomaterials, which are limited by finite EV quantities and potential loss of bioactivity during encapsulation, freeze-thaw cycles, and long-term storage [39]. Active targeting strategies for ischemic stroke have leveraged the pathological upregulation of specific receptors on activated endothelium, including integrin αvβ3, VCAM-1, E-selectin, and P-selectin [40]. The cyclic RGD-4C peptide binds integrin αvβ3 with high affinity and has been successfully used to target various nanocarriers, including liposomes, polymeric nanoparticles, and EVs, to ischemic brain [41]. Our findings extend this concept by demonstrating that intraperitoneally implanted RGD-MSC@Alg was associated with increased EV-associated signal accumulation in the ischemic hemisphere, suggesting that RGD-mediated targeting can function effectively without direct vascular administration.

To achieve this targeted delivery, we selected the intraperitoneal route based on several considerations. The peritoneal cavity provides a large, well-vascularized surface that supports efficient absorption of secreted EVs into systemic circulation while protecting microspheres from mechanical disruption. Intraperitoneal implantation is minimally invasive, well-tolerated, and allows microsphere retrieval if needed. This route has been clinically validated for alginate-encapsulated islet transplantation in diabetes, demonstrating safety and retrievability. Unlike subcutaneous implantation, which risks foreign body reaction and poor vascularization, the peritoneal environment supports sustained cell viability. Intravenous administration of free microspheres carries embolism risk and is unsuitable for larger-diameter implants.

Several aspects of this study warrant discussion regarding functional assessment and safety. First, the functional assessment period was limited to 7 days post-reperfusion. While this timeframe is sufficient to evaluate acute and subacute neuroprotective effects and early motor recovery, it does not permit conclusions regarding long-term functional outcomes or the durability of therapeutic benefit. Ischemic stroke recovery is a dynamic and prolonged process that extends well beyond the first week. Future studies with extended observation periods will be necessary to determine whether the improvements observed with RGD-MSC@Alg implantation translate into sustained long-term functional recovery. Second, we acknowledge several safety considerations associated with persistent implantation of genetically modified MSCs. While alginate encapsulation is designed to provide immune protection, long-term implantation may still elicit foreign body responses, including fibrosis and fibrotic overgrowth, which could compromise EV release and necessitate implant retrieval. The use of RGD-engineered MSCs raises theoretical concerns regarding uncontrolled EV release or potential off-target effects, although no adverse events were observed

during the 7-day study period. The long-term viability of encapsulated MSCs and the consistency of EV production over extended periods also remain to be characterized. Our platform is designed to be retrievable, which mitigates some of these concerns by allowing implant removal if complications arise. However, future studies specifically evaluating peritoneal fibrosis, systemic immune responses, and long-term biosafety in extended observation periods are essential before clinical translation. Third, we acknowledge that several aspects relevant to clinical translation have not been addressed in the current study, including long-term biocompatibility, systemic safety, and manufacturing scalability. While alginate-based encapsulation systems have shown favorable safety profiles in other contexts, such as islet transplantation for diabetes, and while analogous biohybrid devices have advanced to clinical testing, our platform requires substantial additional validation, including long-term implantation studies and large-animal safety assessments before clinical consideration can be proposed.

5. Limitations

Several technical limitations of this study should be acknowledged. First, we did not include a control group receiving blank alginate microspheres containing FK506 alone. FK506 is known to exert direct anti-inflammatory and neuroprotective effects, including suppression of microglial activation and reduction of infarct volume in cerebral ischemia models. However, the total FK506 payload per implant (0.08 mg/kg) is much below the established minimal effective dose for neuroprotection in rodent stroke models (1 mg/kg) [42]. Moreover, the marked therapeutic superiority of RGD-MSC@Alg over MSC@Alg, both sharing the identical FK506-containing matrix, further indicates that the observed benefits are attributable to RGD-targeted EV delivery rather than FK506 leakage. Nonetheless, future studies should incorporate a dedicated FK506-only microsphere control group to formally dissociate local immunomodulation from EV-mediated bioactivity. Second, we acknowledge that tdTomato fluorescence alone does not conclusively demonstrate delivery of intact EVs to brain tissue, as free proteins, membrane fragments, or other fluorescent materials could potentially contribute to the observed signal. While transmembrane-anchored fluorescent proteins represent one of the commonly used and accepted approaches for EV tracking *in vivo* given the current lack of an ideal gold standard method, we recognize this as a limitation. Future studies will seek to incorporate complementary validation techniques such as *in situ* hybridization for EV-encapsulated small RNAs or dual-labeling with additional EV-specific markers to further corroborate our findings. In addition, systemically delivered EVs are known to undergo peripheral sequestration in organs such as the liver, spleen, and lungs, which may reduce the proportion of EVs reaching the ischemic brain. The current study did not quantitatively evaluate EV biodistribution in peripheral organs, representing an additional limitation of the present work. Future studies using quantitative biodistribution approaches will be necessary to further assess tissue-specific EV accumulation and delivery efficiency. Third, only male mice were used in this study. Sex-related differences in stroke pathophysiology are well documented, and our findings may not fully extend to females. While the use of male animals is standard practice in initial proof-of-concept stroke studies to avoid confounding from the estrous cycle, future studies will include female animals to evaluate the translational relevance of our platform across sexes. Fourth, the DIA-based proteomic analysis was performed with a limited number of biological replicates (n = 3 per group). Although the proteomic profiling identified several pathways and proteins potentially associated with the biological effects of sph-EVs, these findings should be considered exploratory and hypothesis-generating rather than definitive mechanistic evidence. In addition, enrichment analyses based on limited sample sizes should be interpreted cautiously. Future studies using larger cohorts and targeted functional experiments will be necessary to validate the biological relevance of the identified pathways and proteins.

6. Conclusions

In summary, we have developed an integrated implantable platform that combines 3D MSC encapsulation, enhanced EV production, and active targeting. The present study provides preliminary proof-of-concept evidence that this system may modulate post-stroke inflammatory responses and improve neurological outcomes in a stroke model. However, long-term therapeutic efficacy, prolonged biosafety, manufacturing scalability, and the potential consequences of chronic implantation remain unresolved and require further investigation before translational or clinical application can be considered.

Availability of Data and Materials

The datasets used and analyzed in this study are available from the corresponding authors upon reasonable request.

Author Contributions

Writing — original draft: YRW. Visualization and formal analysis: YRW and XRL. Investigation: YRW, XRL, XL and YWH. Methodology: XL, YWH and XZ. Supervision, resources, project administration and funding acquisition: XZ and TT. Writing — review & editing and conceptualization: TT. All authors contributed to editorial changes in the manuscript. All authors read and approved the final manuscript. All authors have participated sufficiently in the work and agreed to be accountable for all aspects of the work.

Ethics Approval and Consent to Participate

All animal experiments were conducted in accordance with protocols approved by the Animal Care and Use Committee of Nanjing Medical University (IACUC2411052) and carried out in accordance with institutional guidelines, the ARRIVE 2.0 guidelines, the NIH Guide for the Care and Use of Laboratory Animals, and the Jiangsu Province Regulations on Laboratory Animal Management.

Acknowledgment

The authors would like to thank all members of the laboratory for their valuable support and assistance throughout this study. We also thank the peer reviewers for their constructive comments and suggestions.

Funding

This research was funded by the National Key Research and Development Program of China (2022YFE0132800), the National Natural Science Foundation of China (82271359), and the Key Project of Nanjing Medical University Wuxi Medical Center (WMCJ202402).

Conflicts of Interest

The authors declare no conflicts of interest.

Declaration of AI and AI-Assisted Technologies in the Writing Process

During the preparation of this work, the authors used artificial intelligence tools (ChatGPT, OpenAI, GPT-5.3-mini model) in order to check spelling and grammar. After using this tool, the authors reviewed and edited the content as needed and take full responsibility for the content of the publication.

Supplementary Material

Supplementary material associated with this article can be found, in the online version, at https://doi.org/10.31083/FBL52994.

References

[1] Iadecola C, Buckwalter MS, Anrather J. Immune responses to stroke: mechanisms, modulation, and therapeutic potential. The Journal of Clinical Investigation. 2020; 130: 2777–2788. https://doi.org/10.1172/JCI135530

[2] Chamorro Á, Dirnagl U, Urra X, Planas AM. Neuroprotection in acute stroke: targeting excitotoxicity, oxidative and nitrosative stress, and inflammation. The Lancet. Neurology. 2016; 15: 869–881. https://doi.org/10.1016/S1474-4422(16)00114-9

[3] McMillan N, McMillan A, Kiliaan P, Yahya T, Thakkar R, Weiner H, et al. Stem cell-mediated recovery in stroke: partnering with the immune system. Nature Reviews. Neuroscience. 2026; 27: 23–43. https://doi.org/10.1038/s41583-025-00985-4

[4] Zhang S, Zhang ZY, Sui BD, Zheng CX, Fu Y. The epigenetic landscape of mesenchymal stem cell and extracellular vesicle therapy. Trends in Cell Biology. 2026; 36: 42–56. https://doi.org/10.1016/j.tcb.2025.03.008

[5] Mellado S, Cuesta CM, Montagud S, Rodríguez-Arias M, Moreno-Manzano V, Guerri C, et al. Therapeutic role of mesenchymal stem cell-derived extracellular vesicles in neuroinflammation and cognitive dysfunctions induced by binge-like ethanol treatment in adolescent mice. CNS Neuroscience & Therapeutics. 2023; 29: 4018–4031. https://doi.org/10.1111/cns.14326

[6] Chua JKE, Lim J, Foong LH, Mok CY, Tan HY, Tung XY, et al. Mesenchymal Stem Cell-Derived Extracellular Vesicles: Progress and Remaining Hurdles in Developing Regulatory Compliant Quality Control Assays. Advances in Experimental Medicine and Biology. 2022; 1401: 191–211. https://doi.org/10.1007/5584_2022_728

[7] Ma Y, Dong S, Grippin AJ, Teng L, Lee AS, Kim BYS, et al. Engineering therapeutical extracellular vesicles for clinical translation. Trends in Biotechnology. 2025; 43: 61–82. https://doi.org/10.1016/j.tibtech.2024.08.007

[8] Murali VP, Holmes CA. Biomaterial-based extracellular vesicle delivery for therapeutic applications. Acta Biomaterialia. 2021; 124: 88–107. https://doi.org/10.1016/j.actbio.2021.01.010

[9] Ghanta RK, Aghlara-Fotovat S, Pugazenthi A, Ryan CT, Singh VP, Mathison M, et al. Immune-modulatory alginate protects mesenchymal stem cells for sustained delivery of reparative factors to ischemic myocardium. Biomaterials Science. 2020; 8: 5061–5070. https://doi.org/10.1039/d0bm00855a

[10] Chen T, Liu R, Chen Q, Feng X, Kong B, Zhao Y. MSC-encapsulated porous microparticle eye drops for autoimmune dry eye disease treatment in NOD mice. Science Advances. 2025; 11: eadu9772. https://doi.org/10.1126/sciadv.adu9772

[11] An D, Chiu A, Flanders JA, Song W, Shou D, Lu YC, et al. Designing a retrievable and scalable cell encapsulation device for potential treatment of type 1 diabetes. Proceedings of the National Academy of Sciences of the United States of America. 2018; 115: E263–E272. https://doi.org/10.1073/pnas.1708806115

[12] Desai T, Shea LD. Advances in islet encapsulation technologies. Nature Reviews. Drug Discovery. 2017; 16: 338–350. https://doi.org/10.1038/nrd.2016.232

[13] Orive G, Santos E, Poncelet D, Hernández RM, Pedraz JL, Wahlberg LU, et al. Cell encapsulation: technical and clinical advances. Trends in Pharmacological Sciences. 2015; 36: 537–546. https://doi.org/10.1016/j.tips.2015.05.003

[14] Phan J, Kumar P, Hao D, Gao K, Farmer D, Wang A. Engineering mesenchymal stem cells to improve their exosome efficacy and yield for cell-free therapy. Journal of Extracellular Vesicles. 2018; 7: 1522236. https://doi.org/10.1080/20013078.2018.1522236

[15] Zhu W, Dong Y, Xu P, Pan Q, Jia K, Jin P, et al. A composite hydrogel containing resveratrol-laden nanoparticles and platelet-derived extracellular vesicles promotes wound healing in diabetic mice. Acta Biomaterialia. 2022; 154: 212–230. https://doi.org/10.1016/j.actbio.2022.10.038

[16] Nieland L, Mahjoum S, Grandell E, Breyne K, Breakefield XO. Engineered EVs designed to target diseases of the CNS. Journal of Controlled Release: Official Journal of the Controlled Release Society. 2023; 356: 493–506. https://doi.org/10.1016/j.jconrel.2023.03.009

[17] Tian T, Zhang HX, He CP, Fan S, Zhu YL, Qi C, et al. Surface functionalized exosomes as targeted drug delivery vehicles for cerebral ischemia therapy. Biomaterials. 2018; 150: 137–149. https://doi.org/10.1016/j.biomaterials.2017.10.012

[18] Tian T, Cao L, He C, Ye Q, Liang R, You W, et al. Targeted delivery of neural progenitor cell-derived extracellular vesicles for anti-inflammation after cerebral ischemia. Theranostics. 2021; 11: 6507–6521. https://doi.org/10.7150/thno.56367

[19] Shi V, Wu S, Lian Q, Shi R, Liu Z, Xu T, et al. Dual-Functionalized Extracellular Vesicles Promote Brain Repair and

Remodeling Following Ischemic Stroke in Mice. CNS Neuroscience & Therapeutics. 2025; 31: e70597. https://doi.org/10.1111/cns.70597

[20] Zhu DY, Deng Q, Yao HH, Wang DC, Deng Y, Liu GQ. Inducible nitric oxide synthase expression in the ischemic core and penumbra after transient focal cerebral ischemia in mice. Life Sciences. 2002; 71: 1985–1996. https://doi.org/10.1016/s0024-3205(02)01970-7

[21] Eleftheriadou D, Evans RE, Atkinson E, Abdalla A, Gavins FKH, Boyd AS, et al. An alginate-based encapsulation system for delivery of therapeutic cells to the CNS. RSC Advances. 2022; 12: 4005–4015. https://doi.org/10.1039/d1ra08563h

[22] Mathivanan S, Fahner CJ, Reid GE, Simpson RJ. ExoCarta 2012: database of exosomal proteins, RNA and lipids. Nucleic Acids Research. 2012; 40: D1241–D1244. https://doi.org/10.1093/nar/gkr828

[23] Perucci LO, Sugimoto MA, Gomes KB, Dusse LM, Teixeira MM, Sousa LP. Annexin A1 and specialized proresolving lipid mediators: promoting resolution as a therapeutic strategy in human inflammatory diseases. Expert Opinion on Therapeutic Targets. 2017; 21: 879–896. https://doi.org/10.1080/14728222.2017.1364363

[24] Zhong L, Zhao L, Tang Q, Zhang X, Zhou M, Luo J, et al. Multifunctionality of tissue inhibitor of metalloproteinase-1 in central nervous system diseases. Brain Research Bulletin. 2025; 233: 111647. https://doi.org/10.1016/j.brainresbull.2025.111647

[25] Dixson AC, Dawson TR, Di Vizio D, Weaver AM. Context-specific regulation of extracellular vesicle biogenesis and cargo selection. Nature Reviews. Molecular Cell Biology. 2023; 24: 454–476. https://doi.org/10.1038/s41580-023-00576-0

[26] Soldatov V, Venediktov A, Belykh A, Piavchenko G, Naimzada MD, Ogneva N, et al. Chaperones vs. oxidative stress in the pathobiology of ischemic stroke. Frontiers in Molecular Neuroscience. 2024; 17: 1513084. https://doi.org/10.3389/fnmol.2024.1513084

[27] Morris G, Gevezova M, Sarafian V, Maes M. Redox regulation of the immune response. Cellular & Molecular Immunology. 2022; 19: 1079–1101. https://doi.org/10.1038/s41423-022-00902-0

[28] Ragni E. Extracellular Vesicles: Recent Advances and Perspectives. Frontiers in Bioscience (Landmark Edition). 2025; 30: 36405. https://doi.org/10.31083/fbl36405

[29] Dabrowska S, Andrzejewska A, Janowski M, Lukomska B. Immunomodulatory and Regenerative Effects of Mesenchymal Stem Cells and Extracellular Vesicles: Therapeutic Outlook for Inflammatory and Degenerative Diseases. Frontiers in Immunology. 2021; 11: 591065. https://doi.org/10.3389/fimmu.2020.591065

[30] Wiklander OPB, Brennan MÁ, Lötvall J, Breakefield XO, El Andaloussi S. Advances in therapeutic applications of extracellular vesicles. Science Translational Medicine. 2019; 11: eaav8521. https://doi.org/10.1126/scitranslmed.aav8521

[31] Haraszti RA, Miller R, Stoppato M, Sere YY, Coles A, Didiot MC, et al. Exosomes Produced from 3D Cultures of MSCs by Tangential Flow Filtration Show Higher Yield and Improved Activity. Molecular Therapy : the Journal of the American Society of Gene Therapy. 2018; 26: 2838–2847. https://doi.org/10.1016/j.ymthe.2018.09.015

[32] McArthur S, Juban G, Gobbetti T, Desgeorges T, Theret M, Gondin J, et al. Annexin A1 drives macrophage skewing to accelerate muscle regeneration through AMPK activation. The Journal of Clinical Investigation. 2020; 130: 1156–1167. https://doi.org/10.1172/JCI124635

[33] Crocker SJ, Pagenstecher A, Campbell IL. The TIMPs tango with MMPs and more in the central nervous system. Journal of Neuroscience Research. 2004; 75: 1–11. https://doi.org/10.1002/jnr.10836

[34] Théry C, Witwer KW, Aikawa E, Alcaraz MJ, Anderson JD, Andriantsitohaina R, et al. Minimal information for studies of extracellular vesicles 2018 (MISEV2018): a position statement of the International Society for Extracellular Vesicles and update of the MISEV2014 guidelines. Journal of Extracellular Vesicles. 2018; 7: 1535750. https://doi.org/10.1080/20013078.2018.1535750

[35] Vader P, Mol EA, Pasterkamp G, Schiffelers RM. Extracellular vesicles for drug delivery. Advanced Drug Delivery Reviews. 2016; 106: 148–156. https://doi.org/10.1016/j.addr.2016.02.006

[36] Choi H, Choi Y, Yim HY, Mirzaaghasi A, Yoo JK, Choi C. Biodistribution of Exosomes and Engineering Strategies for Targeted Delivery of Therapeutic Exosomes. Tissue Engineering and Regenerative Medicine. 2021; 18: 499–511. https://doi.org/10.1007/s13770-021-00361-0

[37] Jiang Y, Wang R, Wang C, Guo Y, Xu T, Zhang Z, et al. Brain Microenvironment Responsive and Pro-Angiogenic Extracellular Vesicle-Hydrogel for Promoting Neurobehavioral Recovery in Type 2 Diabetic Mice After Stroke. Advanced Healthcare Materials. 2022; 11: e2201150. https://doi.org/10.1002/adhm.202201150

[38] Shultz RB, Zhong Y. Hydrogel-based local drug delivery strategies for spinal cord repair. Neural Regeneration Research. 2021; 16: 247–253. https://doi.org/10.4103/1673-5374.290882

[39] Jeyaram A, Jay SM. Preservation and Storage Stability of Extracellular Vesicles for Therapeutic Applications. The AAPS Journal. 2017; 20: 1. https://doi.org/10.1208/s12248-017-0160-y

[40] Marcos-Contreras OA, Greineder CF, Kiseleva RY, Parhiz H, Walsh LR, Zuluaga-Ramirez V, et al. Selective targeting of nanomedicine to inflamed cerebral vasculature to enhance the blood-brain barrier. Proceedings of the National Academy of Sciences of the United States of America. 2020; 117: 3405–3414. https://doi.org/10.1073/pnas.1912012117

[41] Danhier F, Le Breton A, Préat V. RGD-based strategies to target alpha(v) beta(3) integrin in cancer therapy and diagnosis. Molecular Pharmaceutics. 2012; 9: 2961–2973. https://doi.org/10.1021/mp3002733

[42] Furuichi Y, Katsuta K, Maeda M, Ueyama N, Moriguchi A, Matsuoka N, et al. Neuroprotective action of tacrolimus (FK506) in focal and global cerebral ischemia in rodents: dose dependency, therapeutic time window and long-term efficacy. Brain Research. 2003; 965: 137–145. https://doi.org/10.1016/s0006-8993(02)04151-3